

## Article

# FBG-Based Accelerometer for Buried Pipeline Natural Frequency Monitoring and Corrosion Detection

Luís Pereira <sup>1,\*</sup>, Israel Sousa <sup>2</sup>, Esequiel Mesquita <sup>2</sup>, Antônio Cabral <sup>2,3</sup>, Nélia Alberto <sup>4</sup>, Camilo Diaz <sup>5</sup>, Humberto Varum <sup>6</sup> and Paulo Antunes <sup>1,4</sup>

<sup>1</sup> I3N & Physics Department, University of Aveiro, 3810-193 Aveiro, Portugal; pantunes@ua.pt

<sup>2</sup> Laboratory of Building Durability and Rehabilitation, Campus Russas, Federal University of Ceará, Russas 62900-000, Ceará, Brazil; israelnlsousa@gmail.com (I.S.); emesquita@ufc.br (E.M.); eduardo.cabral@ufc.br (A.C.)

<sup>3</sup> Department of Structural Engineering and Civil Construction, Campus PICI, Federal University of Ceará, Fortaleza 62900-181, Ceará, Brazil

<sup>4</sup> Instituto de Telecomunicações, University of Aveiro, Campus Universitário de Santiago, 3810-193 Aveiro, Portugal; nelia@ua.pt

<sup>5</sup> Laboratory of Telecommunications, Electrical Engineering Department, Federal University of Espírito Santo, Vitória 29075-910, Espírito Santo, Brazil; camilo.diaz@ufes.br

<sup>6</sup> CONSTRUCT-LESE, Structural Division, Department of Civil Engineering, Faculty of Engineering, University of Porto, 4200-465 Porto, Portugal; hvarum@fe.up.pt

\* Correspondence: Impereira@ua.pt

**Abstract:** Pipelines are structures with great relevance in different industrial sectors and are essential for the proper functioning of the logistics that support today's society. Due to their characteristics, locations, and continuous operation, allied with the huge network of pipelines across the world, they require specialized labor, maintenance, and adequate sensing systems to access their proper operation and detect any damage they may suffer throughout their service life. In this work, a fiber Bragg grating (FBG)-based optical fiber accelerometer (OFA), which was designed and calibrated to operate through wavelength and optical power variations using different interrogation setups, was fixed together with a pair of FBG arrays along a 1020 carbon steel pipeline section with the objective of monitoring the pipeline natural frequency ( $f_{n\_pipeline}$ ) to indirectly evaluate the detection and evolution of corrosion when this structure was buried in sand. Here, corrosion was induced in a small area of the pipeline for 164 days, and the OFA was able to detect a maximum  $f_{n\_pipeline}$  variation of 3.8 Hz in that period. On the other hand, the attached FBGs showed a limited performance once they could successfully operate when the pipeline was unburied, but presented operational limitations when the pipeline was buried in sand. This was due to the inability of the structure to vibrate long enough under these conditions and obtained data from these sensors were insufficient to obtain the  $f_{n\_pipeline}$ .

**Keywords:** fiber Bragg grating; optical fiber accelerometer; buried pipeline; corrosion; natural frequency



**Citation:** Pereira, L.; Sousa, I.; Mesquita, E.; Cabral, A.; Alberto, N.; Diaz, C.; Varum, H.; Antunes, P. FBG-Based Accelerometer for Buried Pipeline Natural Frequency Monitoring and Corrosion Detection. *Buildings* **2024**, *14*, 456. <https://doi.org/10.3390/buildings14020456>

Academic Editor: Jianwen Pan

Received: 9 January 2024

Revised: 31 January 2024

Accepted: 5 February 2024

Published: 7 February 2024



**Copyright:** © 2024 by the authors. Licensee MDPI, Basel, Switzerland. This article is an open access article distributed under the terms and conditions of the Creative Commons Attribution (CC BY) license (<https://creativecommons.org/licenses/by/4.0/>).

## 1. Introduction

Corrosion is often associated with high costs; it is estimated that these costs are, on average, from 3% to 4% of each country's gross domestic product (GDP) [1]. This process is one of the major factors responsible for the deterioration of metallic elements, which can bring about serious economic, environmental, and safety risks, and acts in different ways in different structures [2]. The most common forms of presentation of this corrosion are uniform and pitting, the first being characterized by the evolution of this process along the extension of the entire surface of the metal, promoting a uniform loss of thickness, and the second being characterized by the formation of points in regions located along the metallic element [3–6].

Pipelines are known as the safest and most suitable structures for the transport of fluids, such as flammable gases, however, due to environmental and operational actions, and with the aging of these structures, they end up being susceptible to damage, with corrosion being the main one [7]. Oil and gas pipelines represent great importance from an economic point of view for countries, as well as for guaranteeing social stability [8], but the risks associated with accidents in these structures can compromise a region environmentally and economically due to the strong impact associated with the spillage of material [8,9].

Pipelines can normally be found above the surface (aboveground pipelines) and below (buried pipelines), and together, they are essential for the proper functioning of pipeline transport. On these structures, the greatest amount of damage observed has been identified in buried pipelines, where the highest number of accidents was related to corrosion and material failure, while for aboveground pipelines, this variable was associated with failures in the equipment connected to them [10]. As a result, the development of monitoring techniques for corrosion assessment has been highlighted over the years.

There are numerous techniques for assessing and monitoring metallic structures, especially non-destructive techniques, as Table 1 shows, like the use of ultrasound to assess damage [11–13]. Corrosion monitoring in pipelines, for example, can also involve ultrasonic techniques, such as the use of ultrasonic guided waves (UGW), stress waves that travel great distances and are guided by the limits of the monitored pipeline [14]; however, this presents some limitations, such as the significant influence that external actions can cause, promoting the false indication of defects in these structures [15]. UGWs were also used in the identification of damage in buried pipelines, as proposed in [16], where three different types of damage (gouge, dent, and material loss), in both aboveground and buried pipelines, were simulated and the adequate functioning of UGWs was verified.

Other techniques are highlighted in pipeline monitoring, such as the use of ground penetration radars (GPR) in buried pipeline leak detection [17] and in sensing corrosion in these structures [18]. Normally, the GPRs used in corrosion monitoring are single-polarization systems, which brings about some limitations in their measurements, such as restricted information regarding corrosion products such as the identification of rust and cracks; however, the use of a hybrid-polarization system, as proposed by Liu et al. [19], to detect corrosion in concrete rebar in the early stages, makes it possible to identify this information, but with the limitation of not performing a quantitative assessment.

Radiography is also utilized for corrosion monitoring, as can be seen in [20,21], and it consists of an analysis of the differences in attenuation of the penetrating radiation in materials, depending on their composition, thickness, density, and other aspects [22]. Other studies have used this technique for evaluating corrosion in pipelines, as reported in [23], where the authors utilized two methods for its analysis, tangential radiography and double wall radiography, and concluded that those methods were capable of identifying variations of 10%, 20%, and 50% in the thickness of a pipeline with a 150 mm diameter.

The Eddy currents technique is also a very important method that can be employed for corrosion monitoring [24,25], including in pipelines, as described in [26]. However, this technique can only be applied to unburied pipelines, which is a limitation. Another important technique for corrosion monitoring is thermography [27,28], which analyzes the different heat patterns in a surface and allows for the identification of damages. This method was utilized to assess the reduction in thickness (identified as the result of corrosion) in a steel plate buried in sand [29], allowing for the utilization of this method in buried pipelines, but highlighted the necessity of analyzing the influence of the soil characteristics before application, as this may influence detection.

**Table 1.** Advantages and disadvantages of some of the main techniques to assess corrosion.

Techniques	Advantages	Disadvantages	Reference
Visual inspection	Cheap and easy method	Difficult to detect corrosion in early stages and in difficult access areas	[30]
Ultrasound	Widely disseminated method with high precision	Measurements conducted in small regions and time-consuming process	[11]
Ultrasonic guided waves (UGW)	Able to assess corrosion over long distances in large structures (e.g., pipelines)	External actions can cause a considerable influence that can lead to false indications of defects	[15]
Ground Penetration Radar (GPR)—single-polarization system	Able to indicate damage in buried pipelines	Restricted information regarding corrosion products (e.g., rust and cracks)	[18]
Ground Penetration Radar (GPR)—hybrid-polarization system	Able to detect corrosion products (e.g., rust and cracks)	Does not perform quantitative assessment	[19]
Radiography	Identification of variations in the thickness of 10%, 20%, and 50%	Measurements conducted in small regions and time-consuming process	[23]
Eddy current	Widely disseminated method especially applied for access surface damage	Only applied for unburied pipelines	[26]
Thermography	Able to detect the reduction in the metal thickness	In case of corrosion detection in buried pipelines, it may be necessary to analyze the soil characteristics	[29]
Galvanic sensors	Able to quantify the corrosion in metallic elements	Susceptible to aggressive environments	[31]

In recent years, optical fiber sensors have gained notable prominence in the field of the continuous monitoring of structures [32–35], especially due to the inherent advantages and characteristics of optical fibers, such as immunity to electromagnetic interference, electrical insulation, reduced dimensions, and a low transmission loss, making them suitable to use in aggressive environments. Fiber Bragg gratings (FBGs) have relevant characteristics in the context of monitoring the integrity of structures, such as the possibility of multiplexing several gratings along a single fiber cable, as well as allowing the collection of signals with reduced noise [36]. In this scenario, the use of these sensors has gained interest also due to their easy monitoring and the different parameters that can be measured, such as deformation, frequency, acceleration, temperature, and pressure, among others [37–42]. There are a variety of applications for these sensors to identify damage in pipelines, such as leak detection, as Sun et al. reported, in which the authors proposed a method based on the psychrometer principle with FBG temperature sensors to assess the manifestation of this damage [43]. Also noteworthy are works related to the use of FBGs in corrosion monitoring [44]. In this case, the authors developed hoop-strain FBGs and verified the variation in circumferential strain as a corrosion parameter and suggested further works to evaluate the uniform corrosion in pipes, as well the identification of local corrosion. Ren et al. proposed a distributed system of optical fibers, with FBGs and polyimide-coated optical fibers for corrosion monitoring, also based on circumferential strain variation, obtaining good results, but this system was only applicable in unburied pipelines [45]. Wang et al. proposed an FBG-based optical sensor for monitoring leakage and corrosion in pipelines [46]. Measurements were performed using the theory of analysis of the variation in the internal diameter of the pipeline, which behaves as a pressure container that deforms uniformly under working pressure. The results were promising, showing that the sensor was capable of evaluating the internal corrosion degree in pipelines with an accuracy of 0.1 mm; however, the system still needs to be assessed with a buried pipeline in order to try to simulate a situation closer to the real conditions.

The implementation of accelerometers has gained prominence in the scope of its application in the dynamic monitoring of structures [47–50]. These devices, used in conjunction with optical fiber sensors, have enabled the development of relevant alternatives for structural integrity monitoring. FBG-based optical fiber accelerometers (OFAs) can monitor several parameters related to structural integrity and have been implemented in different types of structures, for example, in a suspended bridge in Malaysia, where an FBG-based OFA array for low-frequency monitoring was used for vibration analysis [51]. On the other hand, Jiang et al. proposed an FBG-based optical accelerometer capable of monitoring the flow of fluid in a pipe, based on the principle of elasticity theory [52]. Although they achieved promising results, limitations were related to external environmental noises, which can influence the collected measurements, as well as the sensor bandwidth, which is capable of monitoring only low frequencies, being susceptible to failure in medium- and high-frequency measurements. Nevertheless, new developments in FBG-based OFA prototypes were achieved to approach these issues and optimize their performance, such as in the case of the work reported by Le et al., where an FBG-based OFA capable of monitoring low and medium frequencies was developed [53]. Also, OFAs can be based on different optical technologies, such as Fabry–Perot interferometry, as Kim et al. proposed, where the natural frequency shift was studied as a function of thickness variation in a low alloy steel piping elbow [54]. Although most investigations have focused mainly on the development of sensors, the study of their application has not been carried out. Thus, the field of OFAs for assessing the evolution of corrosion in buried pipelines is still an object of study worldwide.

In this work, an FBG-based OFA was produced, which, together with two FBG sensor arrays, was used to analyze the impact of induced corrosion on the pipeline natural frequency ( $f_{n\_pipeline}$ ) when this structure was buried in sand. Each FBG sensor array constituted five gratings multiplexed into a single fiber, and while one FBG array was fixed on the coating of the 1020 carbon steel pipeline, the other one was fixed directly on the steel. The OFA performance was initially simulated and experimentally characterized using different interrogation setups for a wavelength and/or optical power-based operation. The purpose of this characterization was to demonstrate that this device could operate with alternative and different monitoring setups, allowing the choice of the most appropriate, easy, and cost-effective acquisition system. Later, the OFA was also fixed to the coating of the pipeline section. The aim of this work was assessing the progress of generalized corrosion, from the beginning, by monitoring the  $f_{n\_pipeline}$  when this structure was buried in sand to simulate the conditions of an underground pipeline. A secondary aim was to analyze and compare the performances of both sensing systems under these conditions to assess their viability in real scenario applications. In the course of the corrosion experiment, the FBG sensors showed sensing limitations, since the vibrations on the buried pipeline section were drastically reduced. In turn, the OFA successfully detected a linear increase in the  $f_{n\_pipeline}$  during the initial stage and a maximum variation of 3.8 Hz, from 265.1 Hz (before the corrosion) to 268.9 Hz (advanced stage of corrosion), showing great potential to monitor the frequencies in buried pipelines or other buried structures, an important parameter for detecting structural damage.

## 2. Materials and Methods

### 2.1. Fiber Bragg Gratings

The implemented monitoring systems are based on FBG technology, an intrinsic optical fiber sensor device. The FBG is a periodic (or quasi-periodic) refractive index modulation along the fiber core. This variation in the refractive index acts as a mirror where partial reflections of the transmitted signal occur, named Fresnel reflections (reflections that occur at the interface between two transparent mediums with different refractive indices). Therefore, the FBG selectively reflects the Bragg wavelength ( $\lambda_B$ ), the wavelength that satisfies the Bragg condition [55]:

$$\lambda_B = n_{eff}\Lambda, \quad (1)$$

where  $n_{eff}$  is the effective refractive index of the optical fiber core and  $\Lambda$  is the period of the refractive index modulation. Since both these parameters are directly affected by external perturbations, such as strain and temperature variations, which consequently leads to  $\lambda_B$  variations, these optical fiber devices are widely used as sensors.

The FBG sensors used in this experiment were produced in two different silica optical fibers, as follows:

- i. two identical FBG arrays inscribed in single-mode GF1AA optical fiber samples (Thorlabs, Newton, NJ, USA), each containing five gratings, which were later fixed to the pipeline section. One array was fixed to the coating (sensors C1 (1532 nm), C2 (1540 nm), C3 (1547 nm), C4 (1554 nm), and C5 (1559 nm)), and the other was fixed to the steel or non-coating areas (sensors NC1 (1532 nm), NC2 (1540 nm), NC3 (1547 nm), NC4 (1554 nm), and NC5 (1559 nm), as Figure 1 shows);
- ii. two FBGs in two different fiber samples and an array with two gratings were inscribed in a single-mode UHNA1 optical fiber (Thorlabs, Newton, NJ, USA) for the OFA. This optical fiber offers low bend losses [56], an important feature for the proposed accelerometer. The two FBGs in different fiber samples were used on different occasions for an initial characterization of the OFA. The array with two FBGs, inscribed in a hydrogenated UHNA1 optical fiber (at a hydrogen pressure of 120 bar for 2 weeks) to enhance the photosensitivity, was used in the final version of the OFA.

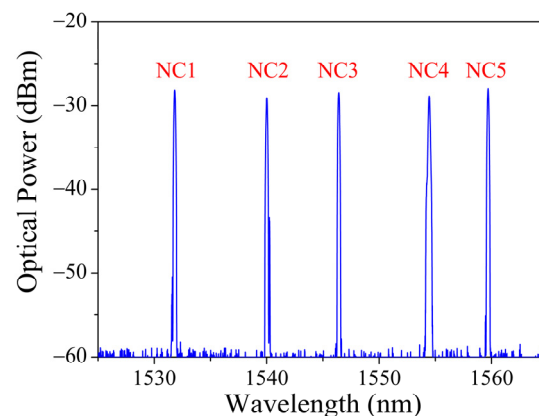


**Figure 1.** Reflection spectrum of the FBG array, which was fixed in the non-coating areas of the pipeline section, with the spectral position and the identification of the sensors.

These FBGs, all 8 mm in physical length, were inscribed by the phase mask method with a pulsed Q-switched Nd: YAG laser system (LS-2137U Laser, LOTIS TII, Minsk, Belarus) emitting at 266 nm, using a pulse frequency of 10 Hz and a pump energy of 25.5 J. More information about the inscription setup can be found in [57,58].

## 2.2. Design and Production of the Optical Fiber Accelerometer

### 2.2.1. Design

The design and dimensions of the proposed OFA are presented in Figure 2a. The mountable/dismountable prototype dimensions are 40 mm in length, 25 mm in width, and 35 mm in height, and the prototype was composed of four different parts: support; upper part; cantilever; and inertial mass. The inertial mass, depicted in Figure 2b, had the shape of a cylinder cut in half with a radius of 8 mm and length of 20 mm. It had an optical fiber groove along the cylindrical surface in the middle of its length and an indentation to insert one end of the cantilever. The other end of the cantilever was then fixed to the accelerometer support (see Figure 2c). This uniaxial accelerometer was specifically designed to incorporate different cantilevers with different dimensions (up to 2 mm in

thickness, which is the width of the indentations in the inertial mass and in the support) and materials, allowing for the manipulation of the acceleration sensitivity ( $S_A$ ) and OFA natural frequency ( $f_{n\_OFA}$ ). Furthermore, this prototype allows for the use of two FBGs, fixed between the support and the inertial mass (one located above and the other below the cantilever), resulting in additional advantages such an increase in the acceleration sensitivity, temperature insensitivity, and possible new interrogation configurations by using twin gratings [59] or even edge filters [57,60] to convert wavelength variations into optical power variations.

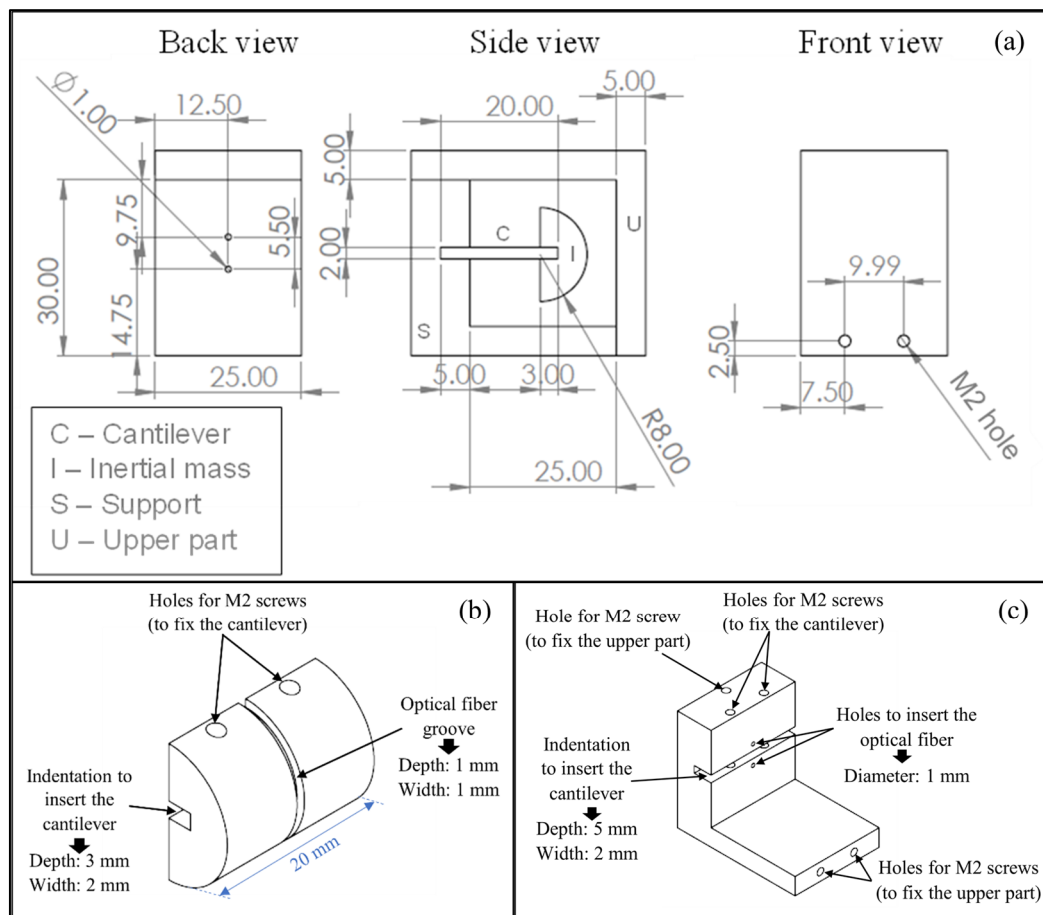


**Figure 2.** (a) Blueprint of the proposed mountable/dismountable optical fiber accelerometer (dimensions in mm); (b) design of the inertial mass; and (c) design of the accelerometer support.

### 2.2.2. Simulations

The design and simulations of the mechanical components of the OFA were performed in SolidWorks, and the mechanical performance in terms of the  $S_A$  and  $f_{n\_OFA}$  was analyzed. Figure 3a,b show the displacement of the inertial mass (made of brass) when subjected to gravitational acceleration ( $1\text{ g} = 9.8\text{ m/s}^2$ ) in the  $x$ -axis ( $\Delta x$ ) and  $y$ -axis ( $\Delta y$ ), respectively, considering the cantilever (made of AISE 316 Stainless Steel) was 20 mm in length and width and 2 mm in thickness. Here, the cantilever was fixed at the end, which was supposed to be connected to the support, while the inertial mass could freely move when an external force was applied. Knowing the displacement in both the  $x$ -axis and  $y$ -axis (plane where the optical fiber would go through along its length and in which the gravity would affect due to the cantilever geometry), it was possible to obtain the estimated  $S_A$  by using the following expression:

$$S_A = \frac{10^6 \Delta L}{L} S_\varepsilon, \quad (2)$$

where  $L$  is the sensing length of the optical fiber in this accelerometer when the FBG was located between the hole of the support and the groove of the inertial mass, and is given by:

$$L \text{ (mm)} = \sqrt{12^2 + 2^2} \quad (3)$$

and  $\Delta L$  is the displacement of the inertial mass when subjected to 1 g, and is obtained by:

$$\Delta L \text{ (mm)} = \sqrt{(12 + \Delta x)^2 + (2 + \Delta y)^2} - L \quad (4)$$

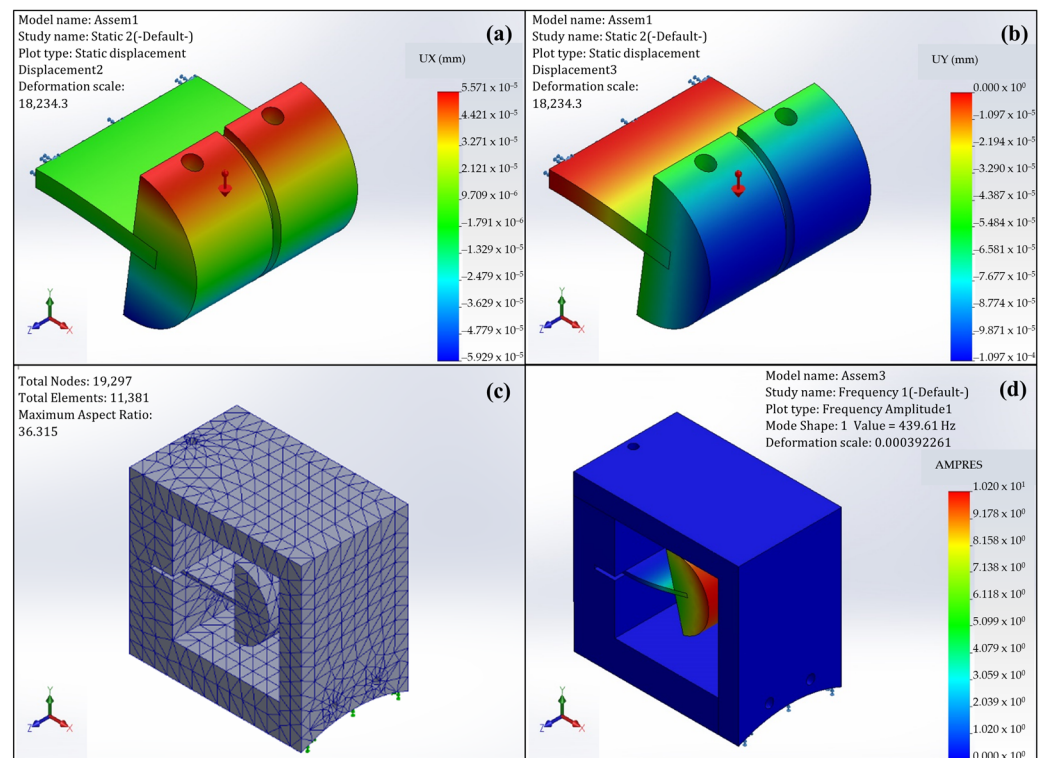


**Figure 3.** Simulation in SolidWorks of the inertial mass displacement when subjected to gravity (cantilever dimensions: 20 mm × 20 mm × 2 mm): (a) in the  $x$ -axis; (b) in the  $y$ -axis; simulation in SolidWorks of the OFA (cantilever dimensions: 20 mm × 20 mm × 0.8 mm): (c) mesh model; and (d) corresponding  $f_{n\_OFA}$ .

$S_\varepsilon$  is the strain sensitivity of the FBGs used in this accelerometer, inscribed in the UHNA1 optical fiber, and after the characterization and linearization, the  $S_\varepsilon$  value was about 1.12 pm/ $\mu\varepsilon$ . On the other hand, the  $f_{n\_OFA}$  was also simulated for the same cantilever dimensions and material as the  $S_A$  simulations. Figure 3c shows the simulated mesh model of the OFA for a cantilever (AISE 316 Stainless Steel) of 20 mm in length and width and 0.8 mm in thickness, composed of 19,207 nodes and 11,381 elements with a maximum aspect ratio of 36.315, while Figure 3d shows the corresponding movement of the first vibrational mode and the  $f_{n\_OFA}$ . These simulations allow us to analyze the appropriate dimensions (and even the appropriate material to obtain an OFA with specific features) of the cantilever to obtain an accelerometer with the desired  $S_A$  and  $f_{n\_OFA}$ . The simulated results of the  $S_A$  and  $f_{n\_OFA}$  are summarized in Table 2, for different cantilever thicknesses between 0.8 and 2 mm.

**Table 2.** Simulated and experimental results regarding the  $S_A$  and  $f_{n\_OFA}$  of the accelerometer for different cantilever dimensions.

Cantilever Dimensions (mm)			Simulated Results		Experimental Results	
Length	Width	Thickness	$S_A$ (pm/g)	$f_{n\_OFA}$ (Hz)	$S_A$ (pm/g)	$f_{n\_OFA}$ (Hz)
20	20	2.0	4.3	1566.5	5.5	1047.0
20	20	1.5	10.3	1030.5	-	-
20	20	1.0	34.1	608.2	-	-
20	20	0.8	65.9	439.6	66.5	374.4

### 2.2.3. Production and Initial Characterization

As mentioned in Section 2.2.1, this OFA prototype was composed of four different parts attached by M2 screws (see Figure 2). In this case, the support and the upper part were made of aluminum and the cantilevers samples were made of AISE 316 stainless steel, while the inertial mass was made of brass. After the simulations and the construction of the accelerometer mechanical parts, the initial experimental characterization of the prototype was performed for two different cantilevers with the same material, the same length and width (20 mm), but different thickness (2 mm and 0.8 mm). A UHNA1 fiber sample with a single FBG was used in each test by fixing the grating between the support and the inertial mass (according to Figure 4). A Luna HYPERION si155 optical fiber interrogator (Luna, Roanoke, VA, USA) was used during this initial characterization, and the results are presented in Table 2.

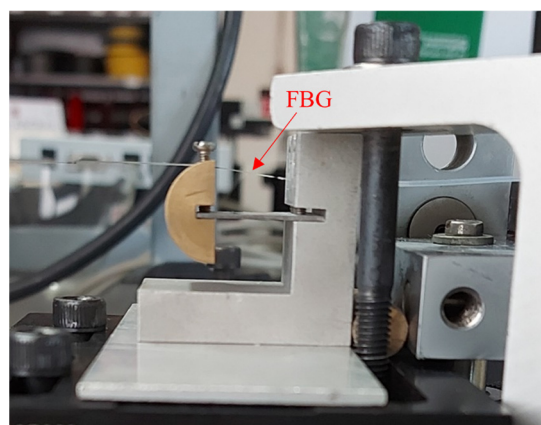


**Figure 4.** Accelerometer prototype (cantilever dimensions: 20 mm × 20 mm × 0.8 mm) during the characterization tests with one FBG attached.

The simulated  $S_A$  values increased exponentially as the thickness of the cantilever decreased. On the other hand, the simulated  $f_{n\_OFA}$  values increased almost linearly as the thickness of the cantilever increased. The experimental results for both cantilevers also demonstrate that trend, and compared with the simulations, they present a good approximation regarding the  $S_A$ , while the  $f_{n\_OFA}$  values have some discrepancy. The differences between the simulated and experimental results, especially for the  $f_{n\_OFA}$ , were for several reasons. Regarding the  $S_A$ , the optical fiber was manually glued to both the support and inertial mass, and depending on the amount of glue and its appliance, the sensing length of the optical fiber with the FBG (distance between the two fixing points) could vary every time an FBG sensor was installed in the accelerometer system, leading to small differences in the  $S_A$  values. Other factors, such as the absence of screws in the simulation and other minor differences regarding the design, contributed to the discrepancy between the  $f_{n\_OFA}$  results. Despite these issues, the simulations allowed us to validate and estimate the performance of the accelerometer before its production. After analyzing both

the simulated and experimental results, the cantilever with a thickness of 0.8 mm (with a much higher  $S_A$ ) was chosen to be incorporated into the final version of the OFA.

The proposed OFA was designed to have two FBGs, as Figure 5a shows, and after the initial characterization of the OFA with a single FBG, a new UHNA1 optical fiber with two FBGs was embedded in the accelerometer. In this configuration, both FBGs were in the same fiber, fixed between the support and the inertial mass and located at opposite sides, one above (FBG 1) and the other below (FBG 2) the cantilever, presenting opposite responses to the movement of the inertial mass. Here, the optical fiber went around the inertial mass through the groove (the bending radius was approximately 7 mm), and the physical distance between the gratings was approximately 25 mm. Figure 5b presents the reflection spectra of the FBGs after straining and attaching them to the accelerometer, according to the scheme presented in Figure 5a.

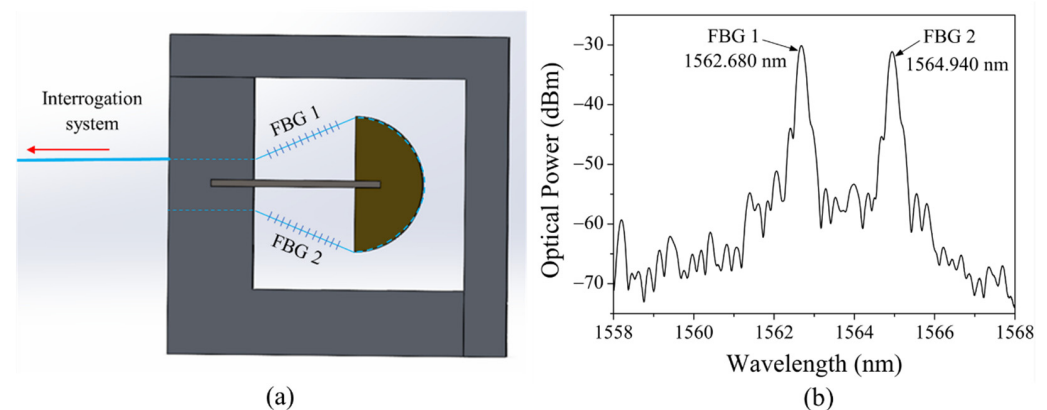


**Figure 5.** (a) Scheme of the OFA. (b) Reflection spectra of the FBGs after attaching them to the accelerometer.

#### 2.2.4. Interrogation Systems

The interrogation systems used to characterize and monitor the OFA performance are shown in Figure 6a,b. Figure 6a presents the static interrogation solution to characterize the OFA, regarding the  $S_A$  performance, in both wavelength and optical power, and besides the OFA and edge filter (an ultra-short FBG (USFBG)), it comprises an amplified spontaneous emission (ASE) broadband light source (model ALS-CL-17-B-FA, Amonics, Hong Kong), two circulators, and an optical spectrum analyzer (OSA) (model MS9740A, Anritsu, Atsugi, Japan). On the other hand, Figure 6b presents the dynamic interrogation solution to measure the vibrations induced in the OFA, where a data acquisition (DAQ) system (composed of a photodetector (model DET01CFC/M, Thorlabs, Newton, NJ, USA), a DAQ device (model USB-6211, National Instruments, Austin, TX, USA), and a computer with the MatLab software (Release 2022a)) were used to monitor the resulting signal and an erbium-doped fiber amplifier (EDFA) (model EDFA100P, Thorlabs, Newton, NJ, USA) could be added to the configuration to amplify the signal from the USFBG. This configuration could be a viable, cost-effective alternative to the commercial interrogators that monitor wavelength variations, and additionally, the data acquisition rate could be easily adjusted to different applications and be much higher (in this case up 120 kHz) when compared with the available interrogators and spectrometers.

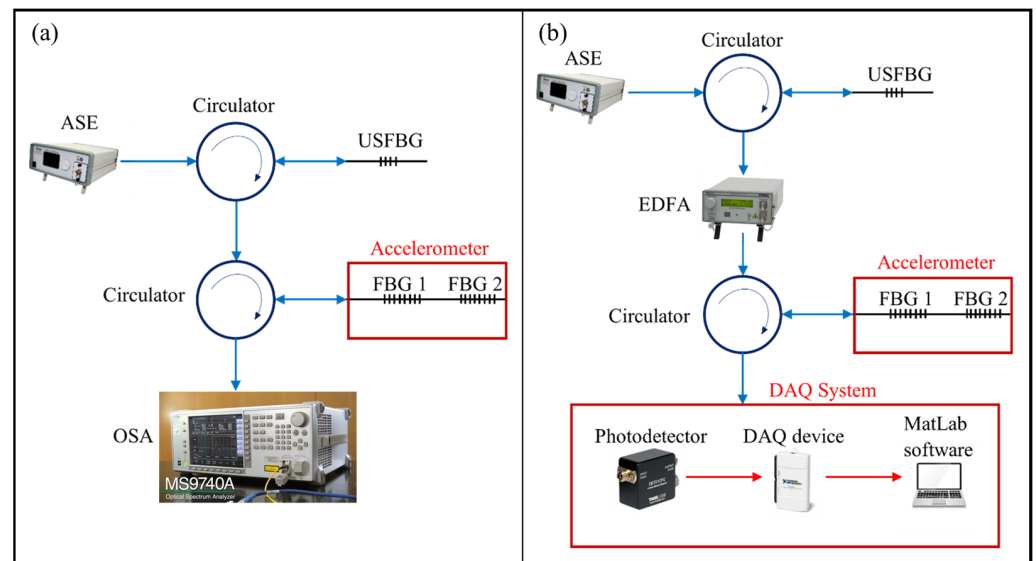


**Figure 6.** Scheme of the setup to interrogate the FBGs from the OFA, using a USFBG as edge filter: (a) for static measurement; (b) for dynamic measurement.

The USFBG, which was used as an edge filter, was produced in a hydrogenated UNHA1 optical fiber sample using a distance between the slit and phase mask of 260 nm and a slit width of 0.5 mm. More details about these gratings and their production procedure can be found in [57]. The optical fiber containing this grating (with a peak wavelength around 1560 nm) was later attached to a fixed and a manual translating stage, which allowed for the calibration of the spectral position of this tunable edge filter.

The Bragg wavelengths of FBG 1 and 2 were around 1562.680 nm and 1564.940 nm (see Figures 5b and 7a), respectively, resulting in a spectral distance between the peaks of approximately 2.260 nm, which was purposely used to obey the requirements of the USFBG filter and take advantage of the opposite responses of the FBGs. To interrogate the FBGs of the accelerometer, the USFBG was strained until the peak wavelength was in the middle of the FBG 1 and FBG 2 reflection wavelengths (around 1563.8 nm), where the reflection signal from those gratings was located at the opposite slopes of the USFBG. The reflected optical signal, measured by the OSA, was obtained using the static measurement setup from Figure 6a. The reflection spectra of the accelerometer's FBGs (black), the USFBG (red), and the resulting signal (blue) are presented in Figure 7a. The acceleration characterization was performed by monitoring the resulting signal spectrum to obtain both wavelength and optical power variations. Figure 7b shows the spectra of the resulting signal for acceleration values of  $-1$  g,  $0$  g, and  $1$  g, while Figure 7c,d show the wavelength and optical power variations, respectively. According to Figure 7c, FBG 1 and FBG 2 had opposite wavelength variation responses, since these gratings were located at opposite sides, and while the movement of the inertial mass stretched one grating, it contracted the other one. The obtained  $S_A$  values were  $32 \pm 1$  pm/g and  $-36 \pm 3$  pm/g for FBG 1 and FBG 2, respectively, and their combined sensitivity ( $\Delta\lambda_{\text{FBG 1}} - \Delta\lambda_{\text{FBG 2}}$ ) was  $68 \pm 4$  pm/g. The sensitivity of each of these gratings was lower than that obtained during the previous characterization (see Table 2), where a single grating was attached to the accelerometer (66.5 pm/g). This could be explained by the layout of the new attached gratings, where the fiber was not only fixed to the support and the inertial mass, but also it went around the inertial mass and was fixed once again in the support, restricting the movements of the mass. Nevertheless, their combined sensitivity was higher compared to the configuration with a single FBG. The optical variations with the acceleration are presented in Figure 7d, where the obtained  $S_A$  values were  $0.56 \pm 0.03$  dB/g and  $0.43 \pm 0.02$  dB/g for FBG 1 and FBG 2, respectively. Due to the location of the FBG 1 and FBG 2 wavelengths in opposite slopes of the USFBG, the simultaneous stretching and contracting of both gratings

from the inertial mass movements led to similar optical power variations (the optical power increased when FBG 1 stretched and/or FBG 2 contracted), resulting in a combined sensitivity of  $0.99 \pm 0.05$  dB/g.

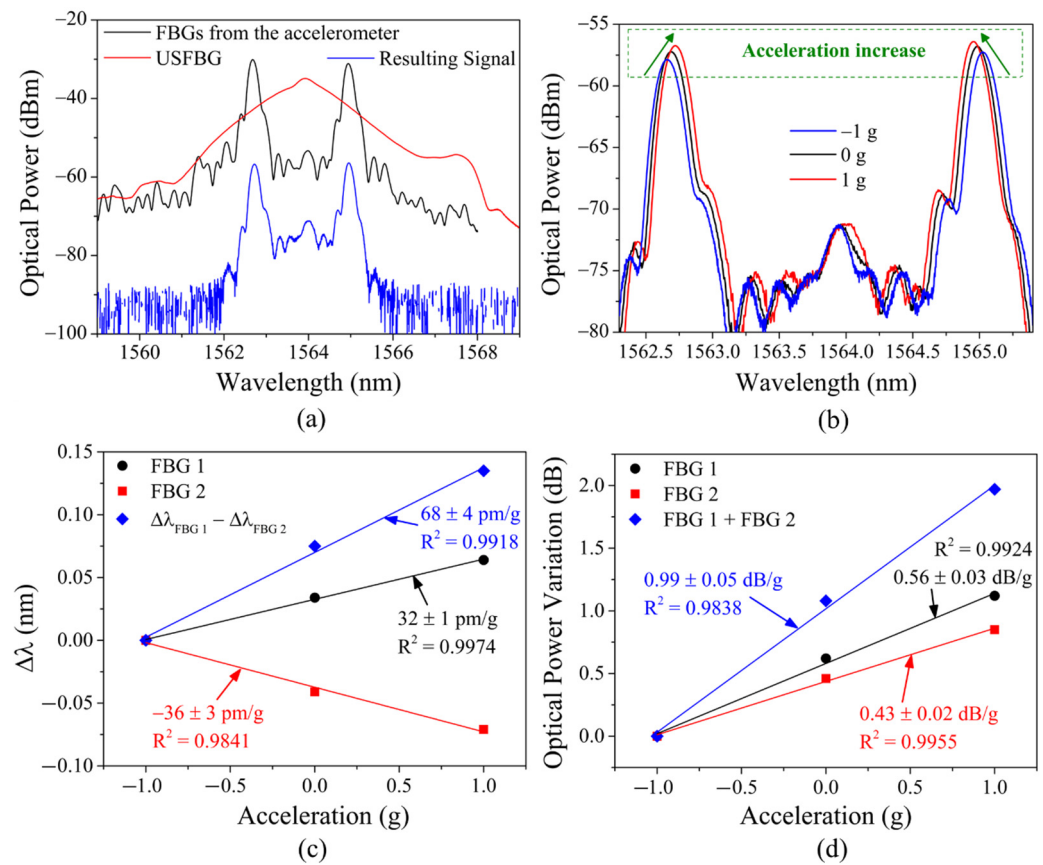


**Figure 7.** (a) Reflection spectra of the accelerometer's FBGs, USFBG, and resulting signal; (b) reflection spectra of the resulting signal for acceleration values of  $-1$  g,  $0$  g, and  $1$  g; (c) Bragg wavelength variations of FBG 1 and FBG 2, and from their combined response, with the acceleration; and (d) optical power variations in FBG 1 and FBG 2, and from their combined response, with the acceleration.

On the other hand, the  $f_{n\_OFA}$  was obtained by inducing vibrations in the inertial mass through the application of a small and sudden force, and for comparison purposes, the measurement was performed in both wavelength (using the Luna HYPERION si155 optical fiber interrogator, with an acquisition frequency of 1 kHz) and optical power variations (using the dynamic measurement setup from Figure 6b, with an acquisition frequency of 5 kHz). The optical power variation monitoring results are shown in Figure 8a, where an  $f_{n\_OFA}$  of 369.7 Hz was determined after the Fast Fourier Transform (FFT) processing of the vibration data. The wavelength results monitored by the interrogator are presented in Figure 8b, and after the data processing, an  $f_{n\_OFA}$  of 369.6 Hz was obtained. The similarity between both  $f_{n\_OFA}$  results demonstrate that this OFA had the capability to operate either with wavelength or optical power variation monitoring, by using, in this case, the interrogator and the dynamic measurement setup from Figure 6b combined with the spectral characteristics of the FBGs from the accelerometer and the USFBG (see Figure 7a), respectively.

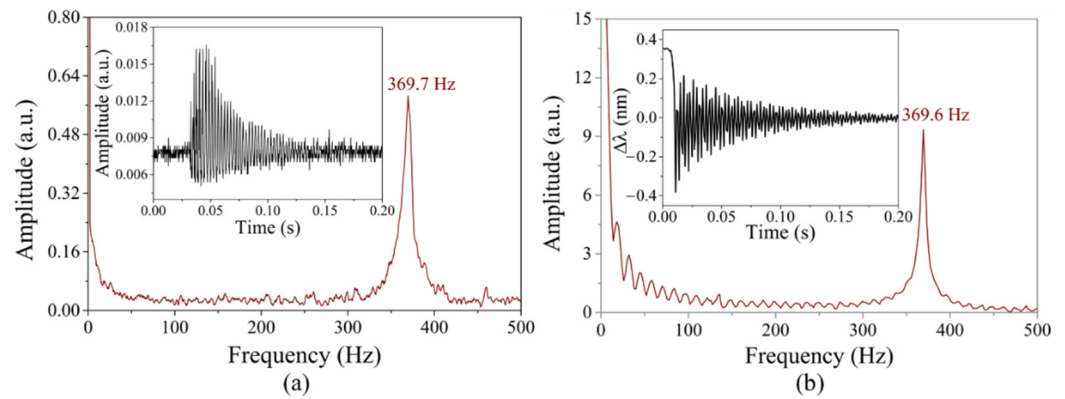


**Figure 8.** Natural frequency response of the OFA by: (a) optical power variation monitoring; and (b) wavelength variation monitoring (inset: obtained data from the induced vibrations, for both cases).

### 2.3. Natural Frequency Monitoring

#### 2.3.1. Principle of Operation

The principle that permits the analysis of the natural frequency of the pipeline section is demonstrated by the following equation [61,62]:

$$f_{n\_pipeline} = \frac{n^2\pi}{2} \sqrt{\frac{EI}{mL^4}}, \quad (5)$$

where  $n$  is the number of modes,  $E$  is the Young's modulus of the pipeline,  $I$  is the moment of inertia of the area,  $m$  is the mass, and  $L$  is the length of the pipeline. The natural frequency is then directly related to the mass and stiffness of the material/structure. Variations in these parameters can be induced by the metal corrosion process, namely, the metal mass loss and changes in geometry due to the reduction in the thickness, which, consequently, leads to stiffness loss.

The vibrations in the pipeline, generated by the transversal impacts, are detected by the attached FBG sensors due to the deformation of the material as it vibrates [63], and they are also detected by the OFA fixed in the pipeline due to the transfer of those vibrations to the inertial mass. The deformations in the pipeline and the movements of the inertial mass cause variations in the Bragg wavelength on the attached FBG sensors and OFA, respectively, allowing for the obtainment of the natural frequencies of this metal structure after FFT processing.

#### 2.3.2. Experimental Procedure

The FBG sensor arrays were distributed and fixed to a 1020 carbon steel pipeline cut in half along its length, with the following dimensions: 707 mm in length, 4 mm in thickness, and 60 mm in diameter. These sensors were fixed with a random strain to the pipeline using X120 adhesive (HBM, Darmstadt, Germany), where each one of the FBGs was embedded in an adhesive layer that was 30 mm in length, 5 mm in width, and 1 mm in height (identified in the black areas on the pipeline). One FBG array was fixed directly in the coating of the pipeline (C1, C2, C3, C4, and C5), while the other was fixed directly in the metal/non-coating (NC1, NC2, NC3, NC4, and NC5), where a paint stripper was utilized to remove the coating in each one of the positions where the five FBG sensors were placed in the pipeline. Figure 9a,b show the position of each one of the sensors along the pipeline section, as well as the location of the OFA and the region where the corrosion will be induced. Each FBG array had three Bragg gratings placed along the direction of the pipeline (C2, C4, C5 and NC1, NC2, NC4) and the two other Bragg gratings placed perpendicular to the pipeline direction (C1, C3 and NC3, NC5).

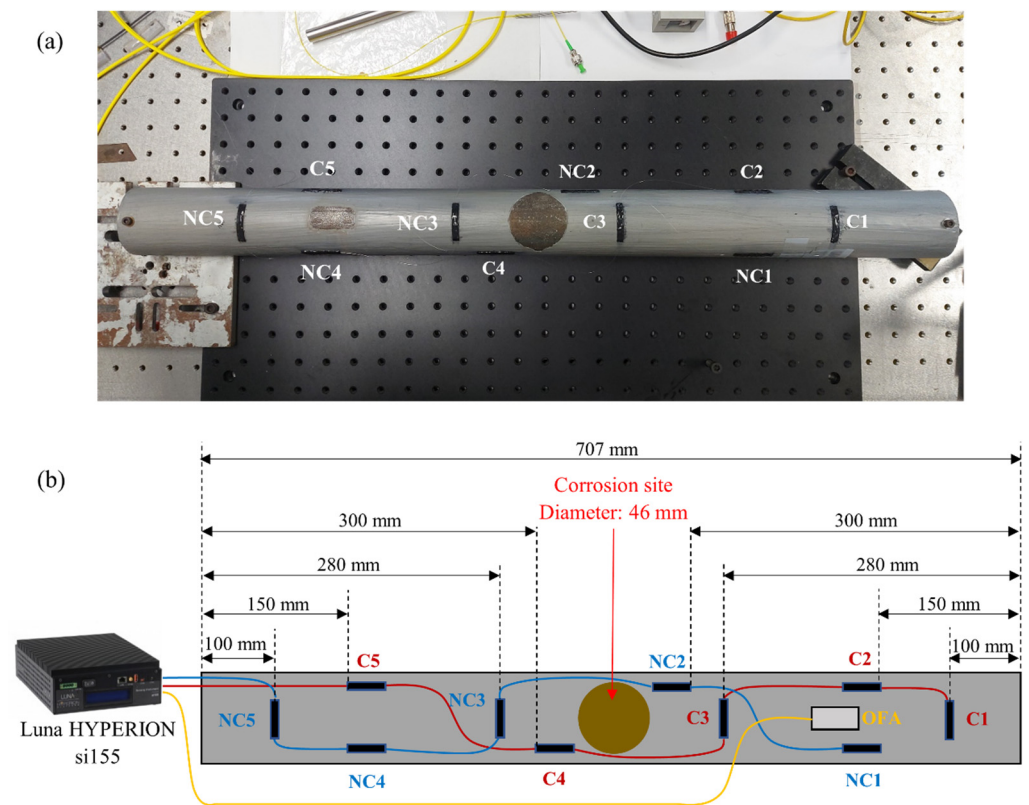


**Figure 9.** (a) Pipeline with the attached FBG sensors; (b) representation of the sensors utilized in the pipeline, as well their specific position.

The corrosion process was induced in an area of approximately  $1662 \text{ mm}^2$  with a  $0.1 \text{ M NaCl}$  solution. The area where the solution was applied had the coating removed with a paint stripper, thus allowing for the direct contact of the solution with the metal. A polyvinyl chloride (PVC) pipe section that was  $125 \text{ mm}$  in height,  $50 \text{ mm}$  in outer diameter, and  $2 \text{ mm}$  in thickness was glued in this area of the pipeline to function as the container to the corrosive solution and to keep the solution in contact with only the predefined area. The OFA, which had the bottom of the support cut in a cylindrical shape along its length ( $60 \text{ mm}$  in diameter) to fit in this metal structure, was glued to the coating of the pipeline, as Figure 10a shows. Figure 10b demonstrates the final layout of the pipeline section with all sensors attached. The monitoring (before, during, and after the corrosion process) of the FBG arrays and the OFA was performed by a Luna HYPERION si155 interrogator with a measurement frequency of  $1 \text{ kHz}$ , as this equipment allowed for the simultaneous measurement of all the sensors' responses, and the acquisition rate was sufficient for characterizing the natural frequencies of this pipeline section. This also simplified the monitoring setup and allowed for a direct comparison of the responses of the sensors. This experimental setup was later placed in a wood box and buried in sand (few centimeters deep) to simulate underground pipelines (see Figure 10c), where only the top part of the PVC container and a small area of the pipeline (to induce vibrations) were left uncovered.

For this study, Bragg wavelength variations were imposed by manually applying multiple vertical impacts in the pipeline (transversally to the pipeline length) with a steel cylinder ( $200 \text{ mm}$  in length and  $13 \text{ mm}$  in diameter). The monitoring was carried out initially without the corrosion process when the setup was fixed to the optical table, and after this step, the measurement was made with the setup buried in the sand for 164 days (a total of 34 measurements during that time span), in which the corrosion solution ( $10 \text{ mL}$  of  $0.1 \text{ M NaCl}$ ) was substituted on each day the measurement was carried out by removing it from the container and adding a new one.

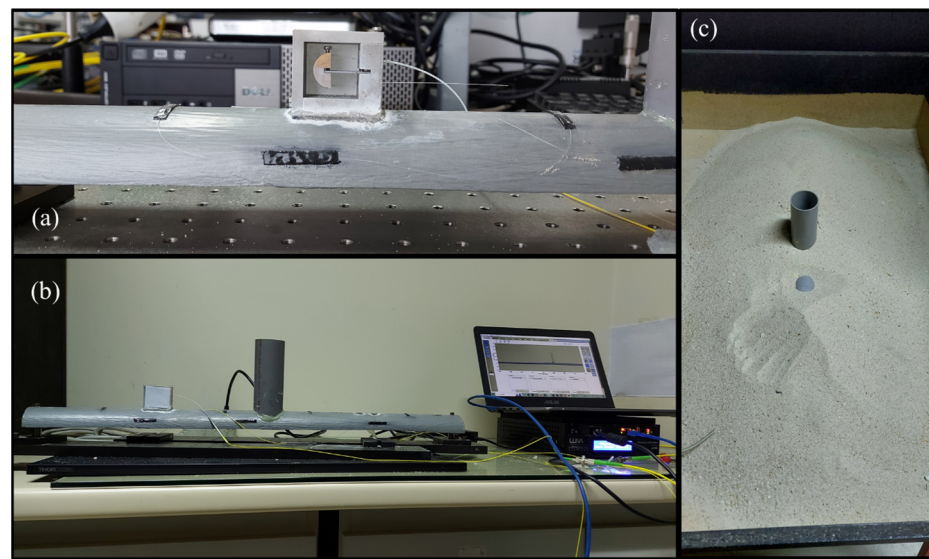


**Figure 10.** (a) Side view of OFA fixed to the pipeline section; (b) side view of the sensors positioned in the pipeline and monitoring system; and (c) the same pipeline section inside the wood box buried in sand to simulate underground pipelines.

### 3. Results and Discussion

By monitoring the buried pipeline, it was possible to compare the efficiencies of the sensors and analyze possible variations in the natural frequencies. Initially, when the setup was fixed to the optical table, all sensors were able to detect the induced vibrations, and with the measured data, obtain the  $f_{n\_pipeline}$ . However, after placing the setup inside the wood box and burying it in the sand, the FBG sensors attached to the pipeline were only able to momentarily detect the impact of the steel cylinder and not the vibrations originated by that impact; thus, it was not possible to process those data to obtain the natural frequencies. On the other hand, the OFA was able to perform this detection, although only one vibrational mode was detected. The possible reasons for these results are associated with the operating principle of the sensors and the deterrent effect of the sand on pipeline vibrations. As the attached FBGs depended on pipeline deformation to identify variations in the Bragg wavelength, the accommodation of the sand used to bury the pipeline, due to its own weight and “soft texture”, decreased the deformation and prevented the maintenance of the induced vibrations for long enough to obtain the frequency results and, therefore, prevented their measurement. This effect was not observed in the OFA, since it works as a spring-mass system where the inertial mass can freely move and detect any vibration in this situation. Figure 11a,b compare the responses of different FBG sensors (C3, C5, NC4, and NC5) to the vertical impact when the pipeline setup was fixed to the optical table and placed in the wood box buried with sand, respectively. In Figure 11a, it is possible to observe that the response of the sensors fixed perpendicular to the pipeline direction (C3 and NC5) had a higher Bragg wavelength variation to the same vertical impact when compared with the response obtained for the sensors positioned in parallel to the pipeline direction (C5 and NC4). Besides the orientation of the FBG sensors, no relevant differences in their response were observable, whether they were fixed above the coating or directly in the metal. On the other hand, the inability of all FBG sensors to monitor the  $f_{n\_pipeline}$  due to the absence of vibrations in the pipeline when it was buried in the sand was noticeable (see Figure 11b). The response of the OFA in those situations is presented in Figure 11c. When the setup was fixed to the optical table, and without the PCV container attached, the vibrations lasted longer and, besides the natural frequency of the OFA, two other distinct frequencies were detected (140.8 Hz and 288.2 Hz), while, when the setup was buried (with the PVC container attached), only one frequency was detected (265.2 Hz). These results demonstrate that different vibrational modes were differently attenuated when the

structure was buried and, even though some modes were no longer detected, others were still able to be monitored by the accelerometers.

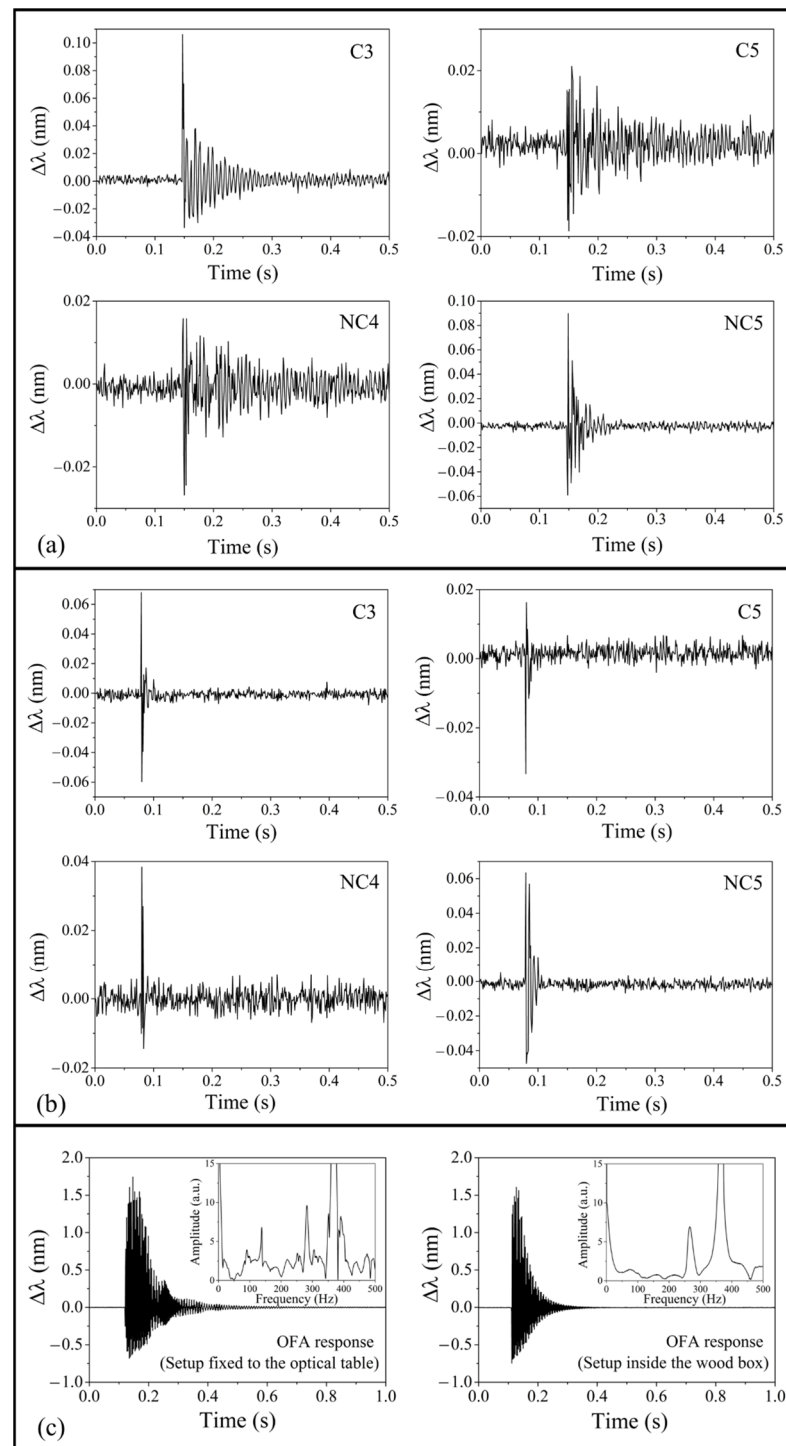


**Figure 11.** Response of the FBG sensors C3, C5, NC4, and NC5 when the pipeline setup was: (a) fixed to the optical table and (b) inside the wood box covered with sand; (c) response of the OFA and the corresponding frequency when the the pipeline setup (without the PVC container attached) was fixed to the optical table (left) and inside the wood box covered with sand (right).

The frequency data of the pipeline at different periods during the corrosion process were measured by the OFA, and through the detected spectrum of frequency, the  $f_{n\_pipeline}$  was monitored. It was possible to visualize a variation associated with the  $f_{n\_pipeline}$  during

the corrosion process, as Figure 12 shows results for days 0, 18 and 164. Here, after the normalization of the  $f_{n\_pipeline}$  amplitude, an increase after 18 days was noticeable.

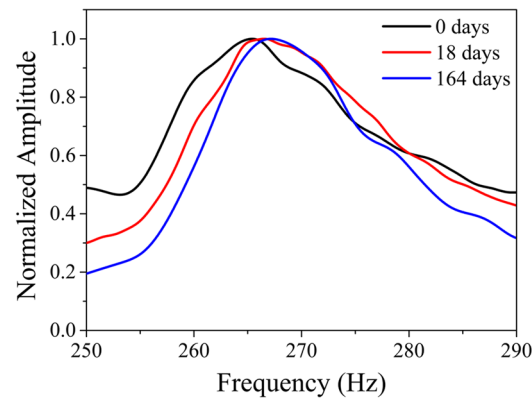


**Figure 12.** Natural frequency behavior of the buried pipeline with normalized amplitude for days 0, 18, and 164.

The collected data during 164 days of monitoring were processed, allowing for the obtainment of the variation in the  $f_{n\_pipeline}$  as a function of time ( $t$ ), as Figure 13 shows. Here, it is possible to identify a linear growth in the first 18 days of monitoring, with the  $f_{n\_pipeline}$  varying from 265.1 to 267.7 Hz during this period, with a respective coefficient of determination equivalent to 94.46%. This linearization is represented by the following equation:

$$f_{n\_pipeline} = 265.05578 + 0.15495t, \quad (0 \leq t \leq 18) \quad (6)$$

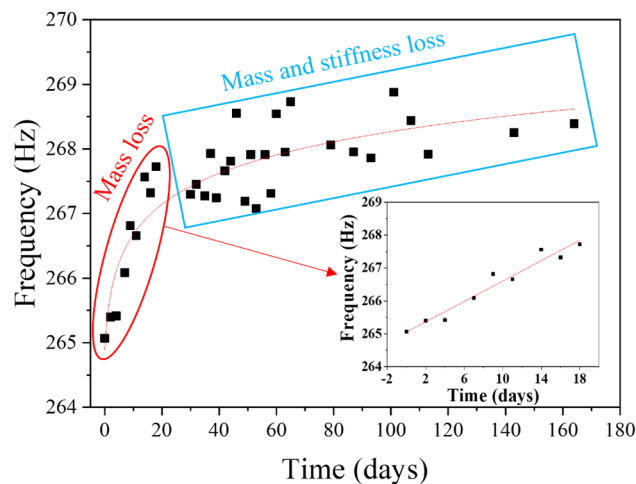


**Figure 13.** Correlation between  $f_{n\_pipeline}$  and time during the entire corrosion experiment.

After 18 days of monitoring, the data started to present another behavior where the  $f_{n\_pipeline}$  values were more dispersed, without the steady growth presented during the first days. Therefore, a logarithm function that better characterizes the behavior of the  $f_{n\_pipeline}$  through the entire corrosion experiment was produced, with a coefficient of determination equal to 77.43% and expressed as:

$$f_{n\_pipeline} = 264.96893 + 0.71528 \ln(t + 0.89996), \quad (0 \leq t \leq 164) \quad (7)$$

This linear growth of  $f_{n\_pipeline}$  in the first 18 days could be related to a major influence from the mass loss, which justifies the quick increase in this time interval. On the other hand, after this period, the growth rate of the  $f_{n\_pipeline}$  started to decrease and the values

became scattered, varying between 267 and 268.9 Hz. This could be related to the variations in the physical properties of the material, in this case, changes in the stiffness of the material with the progression of the corrosion process. Therefore, in this phase, both phenomena (the mass and stiffness losses) contributed to the  $f_{n\_pipeline}$  variations as corrosion occurred (see Figure 13). Figure 14a,b show, respectively, the corrosion site and the mass of the obtained corrosion products measured by a precision scale (model ME104, Mettler Toledo, Greifensee, Switzerland), both after 164 days since the beginning of the experiment. The variation in the mass from the corrosion products during the entire process is presented in Figure 14c. As mentioned previously, at each measurement, the corrosive solution was substituted by removing the solution with corroded material from the container and adding a new one. Later, almost all the liquid of the solution withdrawn from the container was removed and the remaining content went through a drying process. According to Figure 14c, the mass of the corrosion products increased continuously during the experiment, more sharply and linearly as the corrosion process advanced. This allows for the conclusion that, despite the decrease in frequency growth in the advanced corrosion stage, the loss mass still had major effects on the  $f_{n\_pipeline}$ , competing with the stiffness loss in the variation in the natural frequency. It should be noted that the masses of the material from the corrosion process were a bit smaller than the real values, since remnants of this material still remained in the corrosion site, inner part of the PVC tube, pipette, and beaker.

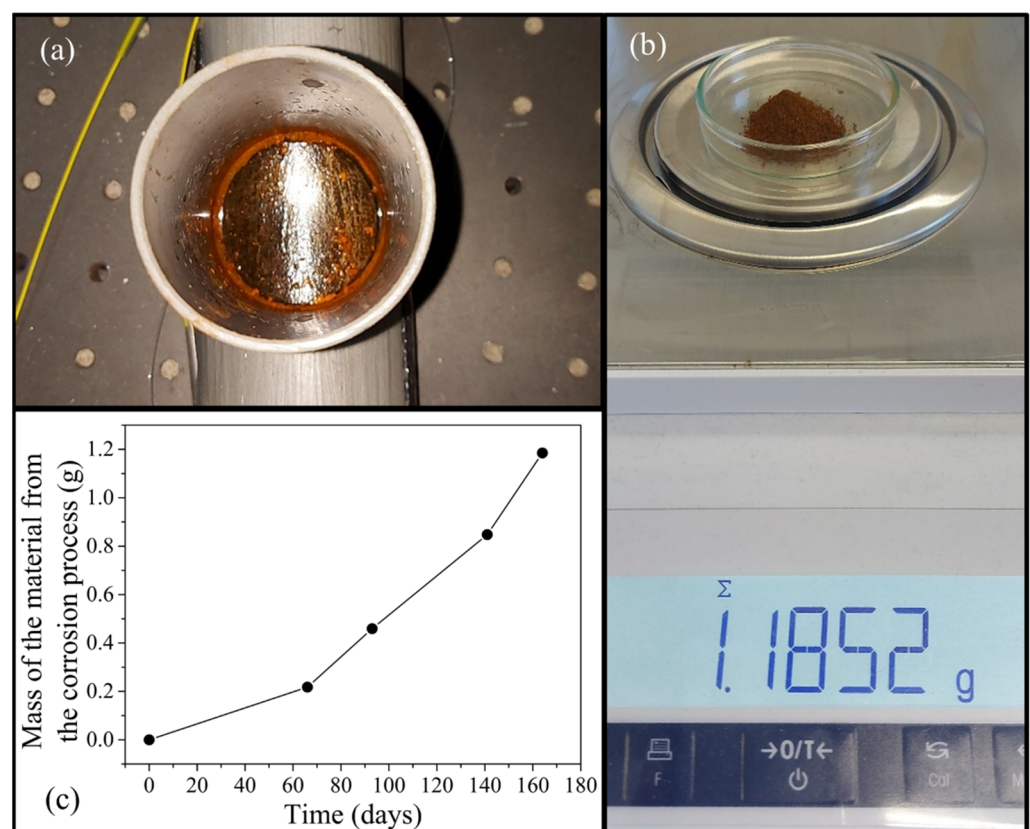


**Figure 14.** (a) Corrosion site after 164 days since the beginning of the corrosion process; (b) mass of the material from the corrosion process after 164 days since the beginning of the corrosion process; and (c) variation in the mass of the material from the corrosion process during the experiment.

The evolution of the  $f_{n\_pipeline}$  before and after the corrosion process, measured by the FBG sensors and the OFA, is presented in Table 3. In situation 1, the setup was fixed to the optical table and all sensors detected two vibrational modes (averaging around 140.5 and 288.4 Hz). In situation 2, the setup was buried inside the wood box and only the OFA was able to measure one of the vibrational modes (265.1 Hz). The  $f_{n\_pipeline}$  variation in

the second mode measured by the OFA in both situations (288.2 to 265.1 Hz) was most likely caused by the attachment of the PVC tube to the pipeline section. In situation 3, the setup was unburied, removed from the wood box, and fixed to the optical table, and here, once again, the FBG sensors were able to measure the  $f_{n\_pipeline}$  values, but the second mode was not detected by these sensors. Regarding the OFA, it was possible for it to detect both vibrational modes in the last situation and, comparing the second mode from situation 2 to situation 3 (see Figure 15), before and after the corrosion process, respectively, the  $f_{n\_pipeline}$  increased by approximately 4.7 Hz.

**Table 3.**  $f_{n\_pipeline}$  at different periods, before and after the corrosion process.

Situation	$f_{n\_pipeline}$ (Hz)										OFA
	C1	C2	C3	C4	C5	NC1	NC2	NC3	NC4	NC5	
1	140.3	140.3	140.3	140.3	140.3	140.5	140.6	140.5	140.6	140.6	140.8
	288.7	288.4	288.2	288.4	288.1	288.4	288.4	288.4	288.4	288.4	288.2
2	-	-	-	-	-	-	-	-	-	-	265.1
3	135.7	135.7	135.7	135.7	135.7	135.7	135.7	135.9	135.7	135.9	135.7
	-	-	-	-	-	-	-	-	-	-	269.8

1—Pipeline setup fixed to the optical table, without the PVC container attached. 2—Pipeline setup inside the wood box buried with sand, with the PVC container attached and before the corrosion process. 3—Pipeline setup fixed to the optical table after the corrosion process.

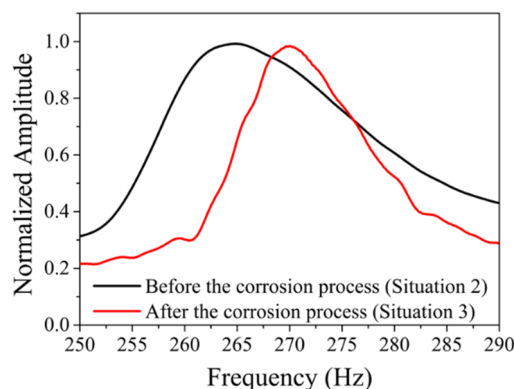


**Figure 15.** Natural frequency spectra of the pipeline setup with normalized amplitude for situations 2 and 3, before and after the corrosion process, respectively.

According to these results, the application of this optical accelerometer has great potential to evaluate frequency variation as a function of corrosion. Therefore, this kind of optical accelerometer can be applied for in situ analyses, especially of buried pipelines, for the continuous assessment of the evolution of corrosion in these structures, especially without the necessity for periodic excavations, and with the operational safety ensured by the utilization of optical fibers, where monitoring systems can be placed far away from the measuring point. On the other hand, although the attached FBG sensors presented a satisfactory response in the initial phase when the setup was outside the wood box, after burying the setup in the sand, they no longer were able to acquire sufficient data to obtain the natural frequencies of the pipeline section. The successful operation of these sensors relies on different factors, in which they permit the structure to deform and vibrate long enough to obtain the corresponding frequencies, and for buried structures, they are not a suitable solution.

#### 4. Conclusions

In this work, a mountable double FBG-based OFA was developed with the capability to operate in both wavelength and optical power variations. In this case, the optical power

was monitored during the OFA characterization by interrogation setups, where a USFBG was used as an edge filter. The dynamic measurement setup used in this work can be a viable alternative to commercial interrogators and spectrometers, with the capability to measure with a much higher acquisition rate than these devices.

This OFA, together with FBG sensors attached to a carbon-steel 1020 pipeline section, was used to measure the  $f_{n\_pipeline}$  when this structure was placed in a wood box buried with sand. The variation in the  $f_{n\_pipeline}$  was analyzed when the pipeline was submitted to localized corrosion, controlled by the utilization of a 0.1 M NaCl solution. During the first 18 days, it was possible to observe linear behavior, with a coefficient of determination equivalent to 94.46%. The correlation between the  $f_{n\_pipeline}$  and time, analyzed over 164 days, started to show non-linear behavior, identified by a logarithmic function, with a determination coefficient of 74.43%. The linear behavior was justified by the greater influence of the mass loss on the variation in the  $f_{n\_pipeline}$  in the first days, and as the corrosion advanced, changes occurred in the metal geometry and physical properties, leading to stiffness loss and a greater contribution of this phenomenon to the  $f_{n\_pipeline}$  variation when compared with the initial phase of corrosion.

On the other hand, the FBG sensors, in which the successful operation was dependent on the capability of the structure to deform and vibrate, were not able to monitor the natural frequency variation in the pipeline, due to the accommodation of the sand used to bury the pipeline and the consequent limitation for the pipeline to vibrate long enough, preventing the monitoring of the natural frequencies by these sensors.

Although the attached FBG sensors were not efficient in detecting the frequency in this situation, and possibly in other buried structures, the OFA was capable of monitoring the evolution of corrosion in the buried pipeline, exemplifying that this kind of accelerometer has great potential to detect and monitor this damage in risky situations and aggressive environments, and can be used as a method that helps in decision making for indirectly identifying corrosion in these buried pipelines, and consequently in the management of these systems. However, these are preliminary results, and further studies and investigations are needed to validate this sensing method and the  $f_{n\_pipeline}$  variation reported in this experiment. In the future, controlled tests where the results of the corroded pipeline are simultaneously compared with the results of an identical uncorroded pipeline, in the same surrounding conditions, can be performed to demonstrate the effectiveness of both the OFAs' capabilities and corrosion-induced frequency variation in underground environments. On the other hand, the use of multiple OFAs at various locations and with different position orientations (parallel and perpendicular to the pipeline longitudinal axis) along the pipeline length could be performed to evaluate, compare, and optimize the sensor configuration performance [64,65]. Additionally, other buried structures (example: complete pipeline sections) can be tested, and the impact of different types of soil and different depths at which the structures are buried can be analyzed.

**Author Contributions:** Conceptualization, E.M. and P.A.; methodology, L.P., E.M. and P.A.; validation, I.S., E.M., A.C., N.A., C.D. and H.V.; formal analysis, L.P., I.S. and E.M.; investigation, L.P. and I.S.; resources, E.M. and P.A.; writing—original draft preparation, L.P. and I.S.; writing—review and editing, E.M., A.C., N.A., C.D., H.V. and P.A.; visualization, L.P.; supervision, P.A. All authors have read and agreed to the published version of the manuscript.

**Funding:** This research was funded by Fundação para a Ciência e Tecnologia of the Ministério da Ciência, Tecnologia e Ensino Superior (FCT/MCTES) through national funds and when applicable co-funded by EU funds under the projects UIDB/50008/2020-UIDP/50008/2020, UIDB/50025/2020, and UIDP/50025/2020. It was also supported by FCT/Ministério da Educação e Ciência (MEC) through national funds and cofunded by a FEDER-PT2020 partnership agreement under the project UID/EEA/50008/2019. The work of Luís Pereira was supported by FCT under grant SFRH/BD/146295/2019. The work of Nélia Alberto was supported by Scientific Employment Stimulus (2022.00250.CEECIND/CP1716/CT0002). The work of Camilo Diaz was supported by FAPES (459/2021) and CNPq (310668/2021-2).

**Data Availability Statement:** The data presented in this study are available on request from the corresponding author.

**Conflicts of Interest:** The authors declare no conflicts of interest.

## References

1. Koch, G. Cost of corrosion. In *Trends in Oil and Gas Corrosion Research and Technologies: Production and Transmission*, 1st ed.; El-Sherik, A.M., Ed.; Woodhead Publishing: Sawston, UK, 2017; pp. 3–30.
2. Gentil, V. *Corrosão*, 3rd ed.; Livros Técnicos e Científicos Editora S.A.: Rio de Janeiro, Brazil, 1996.
3. Sahu, S.; Frankel, G.S. Effect of substrate orientation and anisotropic strength on corrosion pits. *Corros. Sci.* **2023**, *211*, 110772. [[CrossRef](#)]
4. Senior, N.A.; Martino, T.; Diomidis, N.; Gaggiano, R.; Binns, J.; Keech, P. The measurement of ultra low uniform corrosion rates. *Corros. Sci.* **2020**, *176*, 108913. [[CrossRef](#)]
5. Lee, Y.-H.; Byun, J.-H.; Ko, S.-J.; Park, E.-H.; Kim, J.-G. Effect of oxygen on pitting corrosion of copper pipe in fire sprinkler system. *Mater. Chem. Phys.* **2023**, *301*, 127584. [[CrossRef](#)]
6. Zhang, X.; Zhao, S.; Wang, Z.; Li, J.; Qiao, L. The pitting to uniform corrosion evolution process promoted by large inclusions in mooring chain steels. *Mater. Charact.* **2021**, *181*, 111456. [[CrossRef](#)]
7. Teixeira, A.P.; Guedes Soares, C.; Netto, T.A.; Estefen, S.F. Reliability of pipelines with corrosion defects. *Int. J. Press. Vessels Pip.* **2008**, *85*, 228–237. [[CrossRef](#)]
8. Lu, H.; Xi, D.; Qin, G. Environmental risk of oil pipeline accidents. *Sci. Total Environ.* **2023**, *874*, 162386. [[CrossRef](#)] [[PubMed](#)]
9. Ramírez-Camacho, J.G.; Carbone, F.; Pastor, E.; Bubbico, R.; Casal, J. Assessing the consequences of pipeline accidents to support land-use planning. *Saf. Sci.* **2017**, *97*, 34–42. [[CrossRef](#)]
10. Bubbico, R. A statistical analysis of causes and consequences of the release of hazardous materials from pipelines. *The influence of layout. J. Loss Prev. Process Ind.* **2018**, *56*, 458–466. [[CrossRef](#)]
11. Zou, F.; Cegla, F.B. On quantitative corrosion rate monitoring with ultrasound. *J. Electroanal. Chem.* **2018**, *812*, 115–121. [[CrossRef](#)]
12. Sun, X.; Zhang, M.; Gao, W.; Guo, C.; Kong, Q. A novel method for steel bar all-stage pitting corrosion monitoring using the feature-level fusion of ultrasonic direct waves and coda waves. *Struct. Health Monit.* **2023**, *22*, 714–729. [[CrossRef](#)]
13. Thibbotuwa, U.C.; Cortés, A.; Irizar, A. Ultrasound-Based Smart Corrosion Monitoring System for Offshore Wind Turbines. *Appl. Sci.* **2022**, *12*, 808. [[CrossRef](#)]
14. Yaacoubi, S.; El Mountassir, M.; Ferrari, M.; Dahmene, F. Measurement investigations in tubular structures health monitoring via ultrasonic guided waves: A case of study. *Measurement* **2019**, *147*, 106800. [[CrossRef](#)]
15. El Mountassir, M.; Yaacoubi, S.; Dellagi, S.; Sfar, M.; Aouini, M. An ultrasonic guided waves based prognostic approach for predictive maintenance: Experimental study cases. *Mech. Syst. Signal Process.* **2023**, *190*, 110135. [[CrossRef](#)]
16. Ahmad, R.; Banerjee, S.; Kundu, T. Pipe wall damage detection in buried pipes using guided waves. *J. Press. Vessel Technol. Trans. ASME* **2009**, *131*, 011501. [[CrossRef](#)]
17. Gao, L.; Song, H.; Liu, H.; Han, C.; Chen, Y. Model Test Study on Oil Leakage and Underground Pipelines Using Ground Penetrating Radar. *Russ. J. Nondestruct. Test.* **2020**, *56*, 435–444. [[CrossRef](#)]
18. Shokri, N.H.; Amin, Z.M.; Seli, V.A. Non-Destruction Method for Detecting Corroded Underground Pipe Using Ground Penetrating Radar. *IOP Conf. Ser. Earth Environ. Sci.* **2020**, *540*, 012027. [[CrossRef](#)]
19. Liu, H.; Zhong, J.; Ding, F.; Meng, X.; Liu, C.; Cui, J. Detection of early-stage rebar corrosion using a polarimetric ground penetrating radar system. *Constr. Build. Mater.* **2022**, *317*, 125768. [[CrossRef](#)]
20. Wang, X.; Chen, Z.; Guo, E.; Kang, H.; Cao, Z.; Fu, Y.; Wang, T. Corrosion process of Mg–Sn alloys revealed via in situ synchrotron X-ray radiography. *Mater. Lett.* **2022**, *308*, 131139. [[CrossRef](#)]
21. Ewert, U.; Tschalkner, M.; Hohendorf, S.; Bellon, C.; Haith, M.I.; Huthwaite, P.; Lowe, M.J.S. Corrosion monitoring with tangential radiography and limited view computed tomography. *AIP Conf. Proc.* **2016**, *1706*, 110003.
22. Wu, R.; Zhang, H.; Yang, R.; Chen, W.; Chen, G. Nondestructive Testing for Corrosion Evaluation of Metal under Coating. *J. Sens.* **2021**, *2021*, 6640406. [[CrossRef](#)]
23. Edalati, K.Ä.; Rastkhah, N.; Kermani, A.; Seiedi, M.; Movafeghi, A. The use of radiography for thickness measurement and corrosion monitoring in pipes. *Int. J. Press. Vessels Pip.* **2006**, *83*, 736–741. [[CrossRef](#)]
24. He, Y.; Tian, G.; Zhang, H.; Alamin, M.; Simm, A.; Jackson, P. Steel corrosion characterization using pulsed eddy current systems. *IEEE Sens. J.* **2012**, *12*, 2113–2120. [[CrossRef](#)]
25. Butusova, Y.N.; Mishakin, V.V.; Kachanov, M. On monitoring the incubation stage of stress corrosion cracking in steel by the eddy current method. *Int. J. Eng. Sci.* **2020**, *148*, 103212. [[CrossRef](#)]
26. Mardaninejad, R.; Safizadeh, M.S. Gas Pipeline Corrosion Mapping Through Coating Using Pulsed Eddy Current Technique. *Russ. J. Nondestruct. Test.* **2019**, *55*, 858–867. [[CrossRef](#)]
27. Doshvarpassand, S.; Wu, C.; Wang, X. An overview of corrosion defect characterization using active infrared thermography. *Infrared Phys. Technol.* **2019**, *96*, 366–389. [[CrossRef](#)]
28. Elizalde, J.S.G.; Chiou, Y.S. Improving the detectability and confirmation of hidden surface corrosion on metal sheets using active infrared thermography. *J. Build. Eng.* **2023**, *66*, 105931. [[CrossRef](#)]

29. Yu, S.; Chung, W.W.; Lau, T.C.; Lai, W.W.; Sham, J.F.C.; Ho, C.Y. Laboratory validation of in-pipe pulsed thermography in the rapid assessment of external pipe wall thinning in buried metallic utilities. *NDT E Int.* **2023**, *135*, 102791. [[CrossRef](#)]
30. Hren, M.; Kosec, T.; Legat, A. Characterization of Stainless Steel Corrosion Processes in Mortar Using Various Monitoring Techniques. *Constr. Build. Mater.* **2019**, *221*, 604–613. [[CrossRef](#)]
31. Pereira, E.V.; Figueira, R.B.; Salta, M.M.L.; Fonseca, I.T.E. A Galvanic Sensor for Monitoring the Corrosion Condition of the Concrete Reinforcing Steel: Relationship Between the Galvanic and the Corrosion Currents. *Sensors* **2009**, *9*, 8391–8398. [[CrossRef](#)]
32. Tu, G.; Zhang, X.; Zhang, Y.; Ying, Z.; Lv, L. Strain variation measurement with short-time Fourier transform-based Brillouin optical time-domain reflectometry sensing system. *Electron. Lett.* **2014**, *50*, 1624–1626. [[CrossRef](#)]
33. Ma, W.; Jiang, Y.; Zhang, H.; Zhang, L.; Hu, J.; Jiang, L. Miniature on-fiber extrinsic Fabry-Perot interferometric vibration sensors based on micro-cantilever beam. *Nanotechnol. Rev.* **2019**, *8*, 293–298. [[CrossRef](#)]
34. Jin, X.; Sun, C.; Duan, S.; Liu, W.; Li, G.; Zhang, S.; Chen, X.; Zhao, L.; Lu, C.; Yang, X.; et al. High strain sensitivity temperature sensor based on a secondary modulated tapered long period fiber grating. *IEEE Photonics J.* **2019**, *11*, 7100908. [[CrossRef](#)]
35. Ye, X.W.; Ni, Y.Q.; Yin, J.H. Safety Monitoring of Railway Tunnel Construction Using FBG Sensing Technology. *Adv. Struct. Eng.* **2013**, *16*, 1401–1409. [[CrossRef](#)]
36. Rao, Y.-J. In-fibre Bragg grating sensors. *Meas. Sci. Technol.* **1997**, *8*, 355–375. [[CrossRef](#)]
37. Hong, C.; Yuan, Y.; Yang, Y.; Zhang, Y.; Abro, Z.A. A simple FBG pressure sensor fabricated using fused deposition modelling process. *Sens. Actuators A Phys.* **2019**, *285*, 269–274. [[CrossRef](#)]
38. Liu, Z.; Gu, X.; Wu, C.; Ren, H.; Zhou, Z.; Tang, S. Studies on the validity of strain sensors for pavement monitoring: A case study for a fiber Bragg grating sensor and resistive sensor. *Constr. Build. Mater.* **2022**, *321*, 126085. [[CrossRef](#)]
39. Zhao, X.; Jia, Z.; Fan, W.; Liu, W.; Gao, H.; Yang, K.; Yu, D. A Fiber Bragg Grating acceleration sensor with temperature compensation. *Optik* **2021**, *241*, 166993. [[CrossRef](#)]
40. Kokhanovskiy, A.; Shabalov, N.; Dostovalov, A.; Wolf, A. Highly dense FBG temperature sensor assisted with deep learning algorithms. *Sensors* **2021**, *21*, 6188. [[CrossRef](#)]
41. Yan, G.; Wang, T.; Zhu, L.; Meng, F.; Zhuang, W. A novel strain-decoupled sensitized FBG temperature sensor and its applications to aircraft thermal management. *Opt. Laser Technol.* **2021**, *140*, 106597. [[CrossRef](#)]
42. Wang, D.; Wu, Y.; Song, Y.; Wang, Y.; Zhu, L. A double-mass block acceleration sensor based on FBG. *Opt. Fiber Technol.* **2021**, *66*, 102681. [[CrossRef](#)]
43. Sun, M.; Shi, B.; Zhang, D.; Feng, C.; Wu, J.; Wei, G. Pipeline leakage monitoring experiments based on evaporation-enhanced FBG temperature sensing technology. *Struct. Control Health Monit.* **2021**, *28*, e2691. [[CrossRef](#)]
44. Ren, L.; Jia, Z.; Li, H.; Song, G. Design and experimental study on FBG hoop-strain sensor in pipeline monitoring. *Opt. Fiber Technol.* **2014**, *20*, 15–23. [[CrossRef](#)]
45. Ren, L.; Jiang, T.; Jia, Z.; Li, D.; Yuan, C.; Li, H. Pipeline corrosion and leakage monitoring based on the distributed optical fiber sensing technology. *Measurement* **2018**, *122*, 57–65. [[CrossRef](#)]
46. Wang, J.; Ren, L.; Jia, Z.; Jiang, T.; Wang, G. Pipeline leak detection and corrosion monitoring based on a novel FBG pipe-fixture sensor. *Struct. Health Monit.* **2022**, *21*, 1819–1832. [[CrossRef](#)]
47. Shen, N.; Chen, L.; Chen, R. Multi-route fusion method of GNSS and accelerometer for structural health monitoring. *J. Ind. Inf. Integr.* **2023**, *32*, 100442. [[CrossRef](#)]
48. Chilamkuri, K.; Kone, V. Monitoring of varadhi road bridge using accelerometer sensor. *Mater. Today Proc.* **2020**, *33*, 367–371. [[CrossRef](#)]
49. Pieraccini, M.; Fratini, M.; Parrini, F.; Atzeni, C.; Bartoli, G. Interferometric radar vs. accelerometer for dynamic monitoring of large structures: An experimental comparison. *NDT E Int.* **2008**, *41*, 258–264. [[CrossRef](#)]
50. Zhang, H.; Wei, X.; Ding, Y.; Jiang, Z.; Ren, J. A low noise capacitive MEMS accelerometer with anti-spring structure. *Sens. Actuators A Phys.* **2019**, *296*, 79–86. [[CrossRef](#)]
51. Lim, K.-S.; Zaini, M.K.A.; Ong, Z.-C.; Abas, F.Z.M.; Salim, M.A.B.M.; Ahmad, H. Vibration Mode Analysis for a Suspension Bridge by Using Low-Frequency Cantilever-Based FBG Accelerometer Array. *IEEE Trans. Instrum. Meas.* **2021**, *70*, 7000908. [[CrossRef](#)]
52. Jiang, S.; Wang, Y.; Zhang, F.; Sun, Z.; Wang, C. A high-sensitivity FBG accelerometer and application for flow monitoring in oil wells. *Opt. Fiber Technol.* **2022**, *74*, 103128. [[CrossRef](#)]
53. Le, H.-D.; Chiang, C.-C.; Nguyen, C.-N.; Hsu, H.-C. A novel short fiber Bragg grating accelerometer based on a V-type dual mass block structure for low- and medium-frequency vibration measurements. *Opt. Laser Technol.* **2023**, *161*, 109131. [[CrossRef](#)]
54. Kim, J.T.; Seong, S.H.; Lee, C.K.; Hur, S.; Lee, N.Y.; Lee, S.J. Flow-accelerated corrosion monitoring through advanced sensors. *Adv. Sens. Syst. Appl. II* **2005**, *5634*, 404–415.
55. Kashyap, R. *Fiber Bragg Gratings*, 2nd ed.; Academic Press: San Diego, CA, USA, 2009.
56. Ultra-High NA Waveguide Splice Fiber. Available online: [https://www.thorlabs.com/newgrouppage9.cfm?objectgroup\\_id=340](https://www.thorlabs.com/newgrouppage9.cfm?objectgroup_id=340) (accessed on 26 April 2023).
57. Pereira, L.; Min, R.; Woyessa, G.; Bang, O.; Marques, C.; Varum, H.; Antunes, P. Interrogation Method with Temperature Compensation Using Ultra-Short Fiber Bragg Gratings in Silica and Polymer Optical Fibers as Edge Filters. *Sensors* **2023**, *23*, 23. [[CrossRef](#)] [[PubMed](#)]
58. Pereira, L.; Marques, C.; Min, R.; Woyessa, G.; Bang, O.; Varum, H.; Antunes, P. Bragg Gratings in ZEONEX Microstructured Polymer Optical Fiber With 266-nm Nd:YAG Laser. *IEEE Sens. J.* **2023**, *23*, 9308–9316. [[CrossRef](#)]

59. Antunes, P.; Varum, H.; André, P. Uniaxial fiber Bragg grating accelerometer system with temperature and cross axis insensitivity. *Measurement* **2011**, *44*, 55–59. [[CrossRef](#)]
60. Díaz, C.A.R.; Leitão, C.; Marques, C.A.; Domingues, M.F.; Alberto, N.; Pontes, M.J.; Frizera, A.; Ribeiro, M.R.N.; André, P.S.B.; Antunes, P.F.C. Low-cost interrogation technique for dynamic measurements with FBG-based devices. *Sensors* **2017**, *17*, 2414. [[CrossRef](#)] [[PubMed](#)]
61. Demeter, G.F. *Dynamics and Vibration of Structures*; Wiley: New York, NY, USA, 1973; pp. 31–35.
62. Razak, H.A.; Choi, F.C. The effect of corrosion on the natural frequency and modal damping of reinforced concrete beams. *Eng. Struct.* **2001**, *23*, 1126–1133. [[CrossRef](#)]
63. Sousa, I.; Pereira, L.; Mesquita, E.; Souza, V.L.; Araújo, W.S.; Cabral, A.; Alberto, N.; Varum, H.; Antunes, P. Sensing System Based on FBG for Corrosion Monitoring in Metallic Structures. *Sensors* **2022**, *22*, 5947. [[CrossRef](#)]
64. Yang, C.; Liang, K.; Zhang, X.; Geng, X. Sensor placement algorithm for structural health monitoring with redundancy elimination model based on sub-clustering strategy. *Mech. Syst. Signal Process.* **2019**, *124*, 369–387. [[CrossRef](#)]
65. Yang, C.; Xia, Y. Interval Pareto front-based multi-objective robust optimization for sensor placement in structural modal identification. *Reliab. Eng. Syst. Saf.* **2024**, *242*, 109703. [[CrossRef](#)]

**Disclaimer/Publisher’s Note:** The statements, opinions and data contained in all publications are solely those of the individual author(s) and contributor(s) and not of MDPI and/or the editor(s). MDPI and/or the editor(s) disclaim responsibility for any injury to people or property resulting from any ideas, methods, instructions or products referred to in the content.